9th AIAA/CEAS Aeroacoustics Conference and Exhibit
12-14 May 2003, Hilton Head, South Carolina

AIAA 2003-3311

Computational Investigations of High-Speed Dual-Stream Jets

Nicholas J. Georgiadis*
National Aeronautics and Space Administration
Glenn Research Center
Cleveland, Ohio 44135

Dimitri Papamoschou†
University of California, Irvine
Irvine, California 92697-3975

A series of coaxial dual-stream jets issuing into quiescent air was investigated using Reynolds-averaged Navier-Stokes calculations with linear two-equation and nonlinear two-equation explicit algebraic stress turbulence modeling. Comparisons of calculated mean flowfield development were made with experimental data. For all cases, a single axisymmetric convergent-divergent nozzle provided a Mach 1.5 primary flow. Three conical secondary flow nozzles with outer (secondary) to inner (primary) nozzle diameter ratios of 1.4, 1.7, and 2.0 were examined. For each configuration, three subsonic secondary flow Mach numbers (0.37, 0.60, and 0.90) were investigated. A single jet case was also investigated for comparison with the coaxial arrangements. Comparisons of calculated centerline jet velocity decay, velocity profiles in the developing jet region, and potential core lengths yield reasonably good agreement with experimental data. Experimentally observed potential core lengthening with increasing coflow nozzle diameter and increasing secondary flow Mach number is also observed in the calculations. Calculated turbulent kinetic energy fields are provided in order to further characterize the development of the turbulent jet flowfields. The peak kinetic energy magnitude decreases and the location of the peak moves downstream with increasing secondary flow Mach number and increasing secondary nozzle diameter.

Introduction

For several aeronautics research programs in recent years, one of the primary challenges has been to reduce jet noise while maintaining high nozzle thrust levels. On modern commercial aircraft, the most commonly used jet engine is the separate-flow turbofan, with coaxial primary and bypass exhaust streams. At first impression, it may be anticipated that the noise produced by the primary jet in such coaxial configurations could be reduced by a shielding effect due to the secondary (bypass) flow. In Refs. 1 and 2, however, it was shown that the primary jet potential core in coaxial arrangements is actually lengthened, while the secondary stream becomes mixed out well upstream of the end of the primary stream potential core. As a result, a significant portion of the core noise is still emitted by the primary jet stream.

In recent years, a series of experimental investigations on multiple stream jets at the University of California, Irvine (UCI) has investigated alternatives to the coaxial arrangement.[1-5] These include eccentric nozzle configurations, in which the primary (inner) nozzle is translated vertically up to the bypass (upper) nozzle surface. More recently, exhaust nozzle configurations which use vanes installed near the exhaust plane in the bypass duct to deflect the bypass stream have also been investigated. Both of these configurations have been shown to produce significant reduction in noise relative to a coaxial nozzle geometry. In both modified configurations, the noise reduction is accomplished due to a shortening of the primary flow potential core, and an increase in the amount of secondary flow on the underside of the nozzle.

In order to support these experimental studies, a computational effort using Reynolds-averaged Navier-Stokes (RANS) modeling was initiated and will be described in this paper. The focus of the calculations considered initially, and described here, is the more traditional coaxial arrangements, for which the UCI experimental studies have provided an extensive set of velocity profiles for a parametric variation in secondary (bypass) nozzle area and secondary flow Mach number.[1] Comparisons of the RANS calculations are made with the UCI experimental data to determine if the RANS calculations can capture the experimentally observed jet flow development as a function of the

* Research Engineer, Nozzle Branch, Senior Member AIAA.

† Professor and Chair, Department of Mechanical and Aerospace Engineering, Associate Fellow AIAA.

secondary flow area and Mach number. Provided that the computations yield reasonably good agreement with the experimental measurements, the calculations can be used to further examine details of the developing dual-stream jets. In particular, the turbulent kinetic energy fields obtained through the RANS turbulence modeling are investigated in the current study.

Experimental Configurations

All of the coaxial nozzle experiments were conducted in the UCI dual-stream jet facility. The experimental results, and related facilities and procedures, have appeared in an earlier publication (Ref. 1) so here we just give a brief overview. Coaxial nozzle arrangements employed a fixed inner (primary) nozzle and a variety of outer (secondary) nozzles. Air at room temperature was supplied to the primary and secondary nozzles. The primary nozzle had an exit diameter D_P = 12.7 mm and lip thickness of 0.4 mm, and was designed by the method of characteristics for Mach number M_P = 1.5. The Reynolds number of the primary jet was 550,000. Three conical secondary nozzles were used, with exit diameters D_S = 17.8, 21.6, and 25.4 mm. Figure 1 depicts the nozzle configuration for the coaxial arrangement with D_S = 17.8. The primary jet was perfectly expanded and the surrounding air was at ambient, still conditions. The secondary flow was naturally pressure-matched at subsonic conditions. Nozzle configurations and flow conditions are summarized in Tables 1 and 2, respectively. For ease of reference we use a labeling system that describes the size and shape of the secondary nozzle and the Mach number of the secondary flow. Coaxial nozzles are denoted by Cxx where xx = 10 D_S / D_P (the experiment also explored eccentric nozzles, not covered in this paper). The secondary flow is denoted by Myy, where yy = 100 M_S. Case C20M37, for example, describes the coaxial jet with Mach 0.37 secondary flow exhausting from a coaxial arrangement with D_S / D_P = 2.0. The single Mach 1.5 jet is denoted Single.

Table 1. Coaxial Nozzle Configurations

Nozzle	D_S / D_P	A_S / A_P
C14	1.4	0.9
C17	1.7	1.8
C20	2.0	2.9

Pitot probe surveys were conducted at various downstream positions from the jet exit. The inlet of the pitot tube was flattened to an opening 0.2 by 2.0 mm, thus giving a spatial resolution of approximately 0.2 mm. Mach number and velocity profiles were computed from the pitot-pressure profiles under the assumptions of constant static pressure (equal to ambient value) and constant total temperature (equal to room temperature). Radial profiles of pitot pressure were obtained at streamwise locations from D_P = 0 to 20 at increments of D_P = 1. For cases in which a short secondary potential core was expected, particularly with nozzle C14, profiles in the near field of the jet were obtained at finer increments of D_P = 0.25.

Table 2. Flow Conditions

Case	M_P	U_P (m/s)	ρ_P / ρ_∞	M_S	U_S (m/s)	ρ_S / ρ_∞
Single	1.5	430	1.45	0	0	1.00
M37	1.5	430	1.45	0.37	130	1.03
M60	1.5	430	1.45	0.60	210	1.07
M90	1.5	430	1.45	0.90	290	1.16

Computational Method

The Reynolds-averaged Navier-Stokes (RANS) solver used in this study is WIND[6] - Version 5, the production flow solver of the NPARC Alliance, a joint code development group of NASA Glenn Research Center, USAF Arnold Engineering Development Center, and the Boeing Company. WIND is a structured-grid finite volume code using upwind numerics for most flow applications, and in the current study, the flux difference-splitting technique of Roe was employed to calculate fluxes at cell faces. A broad set of turbulence models are available, all of which fall into the class of eddy-viscosity formulations. In the current study, two linear two-equation and one nonlinear two-equation explicit algebraic stress model (EASM) formulations are employed to calculate the jet flows. No corrections for compressibility or other jet effects are employed in this study. The linear two-equation models used here are the k-ε model of Chien[7] and the shear-stress transport (SST) model of Menter[8,9]. The SST model employs a k-ω formulation in the inner region of wall boundary layers and switches to a transformed k-ε formulation in the outer region of boundary layers and in free shear layer/mixing regions. An explicit algebraic Reynolds stress model (EASM) based upon the work of Rumsey, et al.,[10,11] has recently been installed in WIND[12] to improve the capability to calculate compressible jet flows. Unlike linear two-equation models, EASM formulations are sensitive to turbulent stress anisotropies and have a direct relation to the full Reynolds stress model. As a result, EASM models have the capability to include more relevant flow physics than the linear models. However, they are also solved using a two-equation approach and as a result are not significantly more computational expensive than linear two-equation models.

Computational Grids and Boundary Conditions

Computational grids for the single and coaxial nozzles were constructed as follows. Since all of the calculations discussed here were run using WIND in axisymmetric mode, two-dimensional grids were employed. For the single jet nozzle, a three zone grid was constructed having 33,423 total points. The three zones consisted of the primary jet internal nozzle region, ambient air inflow, and downstream plume region. For each of the three coaxial nozzle configurations listed in Table 1, a four zone grid was constructed having 49,172 total points. The four zones consisted of the primary jet internal nozzle region, secondary flow internal nozzle, ambient air inflow, and downstream plume region. Figure 2 shows details of the axisymmetric grid for the C20 coaxial nozzle near the nozzle exit plane. For all of the single and coaxial nozzle cases investigated here, the grids extended 60 D_P downstream of the nozzle exit and 24 D_P vertically from the axis of symmetry.

For each of the nozzle grids, internal nozzle walls were packed to the solid surfaces such that the average y+ of the first point off the wall was approximately 1. Additionally, each of the grid zones was packed axially to the nozzle exit plane. During the course of each of the calculations discussed here, grid sequencing was employed with WIND in order to accelerate convergence. This grid sequencing procedure also enabled a grid sensitivity examination where the intermediate solution obtained with every other grid point in each computational direction (coarse) was compared with the final solution obtained with the fine grid. In every case, the coarse grid and fine grid solutions were very similar. For all of the results discussed in the next section, the fine grid solutions are provided.

The inflow boundaries of the primary and secondary nozzle flows specified the nozzle stagnation pressure that corresponds to the ideally expanded Mach number of the flow conditions shown in Table 2. The stagnation temperature was set to the ambient static temperature in order to correspond to the conditions of the experiment. The downstream static pressure was set to the ambient pressure.

Results

Turbulence Model Variations

The three turbulence models discussed in the Computational Methods section were used to calculate each of the nozzle cases in order to provide an assessment of turbulence model effects on prediction of the dual-stream jet characteristics. In each of these calculations, it was noted that the turbulent boundary layers developing inside the primary nozzle resulted in a slightly under-expanded flow condition at the nozzle exit, where the calculated exit plane Mach number, approximately 1.45 for each of these cases, was lower than the design exit Mach number = 1.5. This was the result of the turbulent boundary layer displacement thickness reducing the effective area ratio of the nozzle exit station to the nozzle throat. As a result, a fourth set of calculations was obtained by running the SST model with laminar specification inside the primary and secondary nozzles. Downstream in the jet plume region, the SST model was employed as with the standard case. These calculations obtained with laminar walls resulted in a nearly perfectly expanded nozzle, with the primary nozzle exit Mach number very close to 1.5. As a result of this extra simulation, a total of four turbulence model approaches were employed: (1) SST with turbulent wall boundary layers, (2) SST with laminar wall boundary layers, (3) k-ε with turbulent wall boundary layers, and (4) EASM with turbulent wall boundary layers.

Figure 3(a) provides a comparison of the centerline velocity decay using all of the modeling approaches. It may be observed that all of turbulence models capture the core flow decay reasonably well, although all of the calculations overpredict the jet decay rate. In Fig. 3(b) the maximum turbulent kinetic energy at each axial station is shown. This was obtained by surveying each vertical grid line starting from the axis of symmetry. While no experimental data is available for comparison, it may be observed that the three linear two-equation turbulence model approaches indicate a higher initial turbulence peak than that obtained from the EASM.

The centerline velocities and maximum turbulent kinetic energy comparisons for one of the coaxial cases, the largest secondary nozzle geometry with Mach 0.60 secondary flow (C20M60), is shown in Fig. 4. Here it may be observed that each of the linear two-equation models predicts the lengths of the primary jet potential core in close agreement to the experimental data, while the EASM solution indicates a significantly longer potential core. Examining the maximum turbulent kinetic energy predictions in Fig. 4(b), the locations of the peak turbulent kinetic energy just downstream of the end of the potential cores correspond to the centerline velocity decay results of Fig. 4(a), with the most noticeable result being the lagging of the EASM solution behind that of the linear two-equation models. It may be noted that for all of the results presented in Figs. 3 and 4, there are no notable differences between the standard SST calculations and the calculations using the modified SST approach with laminar walls, except for differences just downstream of the nozzle exit plane.

The qualitative agreement of the calculations using the four turbulence modeling approaches for the

other coaxial configurations and secondary flow Mach numbers is similar to that of the C20M60 results shown in Fig. 4. In the interest of space, all of these results are not presented in this paper. However, a comparison of the primary flow potential core lengths obtained from the experiment and calculations for each of the ten flow cases is presented in Table 3. The primary jet potential core length, L_P, is defined as the distance from jet exit to the axial station where the centerline velocity is 90 percent of the primary nozzle exit velocity. The results shown in Table 3 indicate that the three linear two-equation turbulence model approaches indicate reasonably close agreement with the experimental data. The Chien k-ε results indicate a slightly shorter core than the SST solutions (which also uses a k-ε formulation in the jet region) due to minor differences in the closure coefficients of the respective k-ε models. The potential cores of the SST and SST (laminar boundary layers) solutions are extremely similar, indicating that the differences in the upstream wall boundary layers and resulting state of the primary jet core flow at the nozzle exit are not as significant as jet mixing effects.

Table 3. Potential Core Length Comparisons

Case	Expt.	SST	SST (lam.)	k-ε	EASM
Single	9.2	10.4	10.4	9.0	11.5
C14M37	10.5	10.5	10.5	9.6	12.5
C14M60	11.4	11.4	11.3	10.2	13.4
C14M90	12.5	12.2	12.1	11.1	14.8
C17M37	11.4	11.2	11.1	10.7	13.9
C17M60	13.3	12.9	12.7	11.8	15.7
C17M90	15.1	14.4	14.3	13.3	18.3
C20M37	12.3	11.8	11.7	11.0	14.0
C20M60	13.8	14.2	14.1	13.4	17.9
C20M90	15.5	16.6	16.5	15.5	21.6

It may be noted that the EASM solutions indicate significantly longer potential cores than those of the other turbulence models and the experimental data. Despite the greater sophistication of the EASM, similar results were obtained in Ref. 13 for lobed nozzle calculations. It was concluded that a recalibration of the particular EASM used there (same model used in this paper) for jet mixing problems was required, as is supported by these results. Following such a recalibration, the benefits of the EASM, in particular the capability to model turbulent flow anisotropies, may be realized.

Based upon these comparisons, we conclude that the linear two-equation models are able to accurately reproduce the qualitative characteristics of the coaxial jets for the flow conditions examined herein. In the next section, more detailed comparisons and examination of the effects of secondary flow area and Mach number are investigated using the standard SST model, which provided the overall best agreement with experimental data and yielded the best convergence characteristics.

Detailed Flow Comparisons

Axial velocity contours for the reference single jet case and the largest secondary nozzle (C20) for all of the secondary flow conditions are provided in Fig. 5. For purposes of comparison with the coaxial cases, the single jet case may be considered as a "coaxial configuration" with secondary Mach number set to 0. It may be observed that as the secondary Mach number is increased, the length of the primary jet potential core is lengthened, as expected. For the case with secondary Mach number set to 0.90 in Fig. 5(d), it is interesting to note that the initial jet region is characterized by some mild expansion and compression waves, which is not as evident in the other cases. This is believed to be due to the nearly sonic state of the secondary flow resulting in the primary jet not being able to immediately settle out to the ambient static pressure.

Turbulent kinetic energy contours for the same four cases are provided in Fig. 6. Here it is noted that as the secondary flow Mach number is increased, the peak magnitude in turbulent kinetic energy is reduced and the location of the peak moves downstream.

Further comparisons of the primary potential core lengths predicted by the SST solutions and the experimental data, defined in the previous section, are provided in Fig. 7. Comparisons of the sonic lengths, L_*, defined as the distance from jet exit to the axial station where the centerline Mach number reaches 1.0, are provided in Fig. 8. Figs. 7 and 8 indicate that the calculations are able to reproduce the qualitative trends of variations in potential core and sonic length with secondary flow area and Mach number.

Detailed comparisons of velocity profiles are provided for the single jet in Fig. 9 and the C20 coaxial nozzles in Fig. 10 at 5 axial stations in the jet development region. Note that the last experimental measurement station available for the single jet corresponded to $x/D_P = 20$, while for the C20 cases, the last measurement station was at $x/D_P = 18$. These comparisons further indicate the overall good agreement between calculations provided by the SST linear two-equation turbulence model and the experimental data.

Utilizing the confidence built from the qualitative agreement of the computations with experiment, we finally consider variations in the jet decay behavior of all the coflow configurations (secondary nozzle configuration and Mach number) while examining only the computations. Figure 11 provides variation in the centerline axial velocity decay

with secondary Mach number for each of the three coaxial nozzle configurations. As is expected, variations in jet decay with secondary Mach number become greater with increasing secondary flow area. Comparisons of the maximum turbulent kinetic energy are provided in Fig. 12. For each of the configurations, as the secondary Mach number is increased, the peak kinetic energy is observed to decrease and the location of the peak moves downstream.

Concluding Remarks

The results of this study indicate that RANS calculations employing linear two-equation turbulence modeling, can predict the development of high-speed coaxial jets reasonably well. It should be noted that all of the jets investigated here were unheated, and temperature effects have been shown to be an added complexity for which computational models still need development. However, for cases investigated here for an unheated supersonic primary jet with a series of secondary Mach number and secondary nozzle area variations, the computations were able to reproduce the experimental observations of primary jet potential core lengthening with increasing coflow nozzle area and increasing coflow Mach number. Comparisons of computed and experimentally measured velocity profiles also indicted reasonably close agreement.

The confidence established in the computational approach enabled the examination of turbulent kinetic energy in the developing jets, which was computed, but not measured experimentally. It was observed that peak kinetic energy magnitude decreased and the location of the peak moved downstream with increasing secondary flow Mach number and increasing secondary nozzle diameter. Finally, we can conclude that the computational methods demonstrated here should be able to be successfully used in future calculations of non-traditional dual-stream jets such as eccentric arrangements and configurations with deflected bypass streams.

References

1. Murakami, E. and Papamoschou, D., "Mean Flow Development in Dual-Stream Compressible Jets," *AIAA Journal*, Vol. 40, No. 6, June 2002, pp. 1131-1138.
2. Papamoschou, D., "Noise Suppression in Moderate-Speed Multistream Jets," AIAA Paper 2002-2557, June 2002.
3. Papamoschou, D. and Debiasi, M., "Directional Suppression of Noise from a High-Speed Jet," *AIAA Journal*, Vol. 39, No. 3, March 2001, pp. 380-387.
4. Papamoschou, D. and Debiasi, M., "Mach Wave Elimination Applied to Turbofan Engines," AIAA Paper 2002-0368, Jan. 2002.
5. Papamoschou, D., "Engine Cycle and Exhaust Configurations for Quiet Supersonic Propulsion," AIAA Paper 2002-3917, July 2002.
6. Nelson, C.C. and Power, G.D., "CHSSI Project CFD-7: The NPARC Alliance Flow Simulation System," AIAA Paper 2001-0594, Jan. 2001.
7. Chien, K.-Y., "Predictions of Channel and Boundary Layer Flows with a Low-Reynolds-Number Turbulence Model," *AIAA Journal*, Vol. 20, No. 1, Jan. 1982, pp. 33-38.
8. Menter, F.R., "Two-Equation Eddy-Viscosity Turbulence Models for Engineering Applications," *AIAA Journal*, Vol. 32, No. 8, Aug. 1994, pp. 1598-1605.
9. Menter, F.R., "Zonal Two-Equation k-ω Turbulence Models for Aerodynamic Flows, AIAA Paper 93-2906, July 1993.
10. Rumsey, C.L., Gatski, T.B., and Morrison, J.H., "Turbulence Model Predictions of Strongly Curved Flow in a U-Duct," *AIAA Journal*, Vol. 38, No. 8, 2000, pp. 1394-1402.
11. Rumsey, C.L. and Gatski, T.B., "Recent Turbulence Model Advances Applied to Multielement Airfoil Computations," *J. Aircraft*, Vol. 38, No. 5, Sept. 2001, pp. 904-910.
12. Yoder, D.A., "Initial Evaluation of an Algebraic Reynolds Stress Model or Compressible Turbulent Shear Flows," AIAA Paper 2003-0548, Jan. 2003.
13. Georgiadis, N.J., Rumsey, C.L., Yoder, D.A., and Zaman, K.B. M. Q., "Effects of RANS Turbulence Modeling on Calculation of Lobed Nozzle Flowfields," AIAA Paper 2003-1271, Jan. 2003.

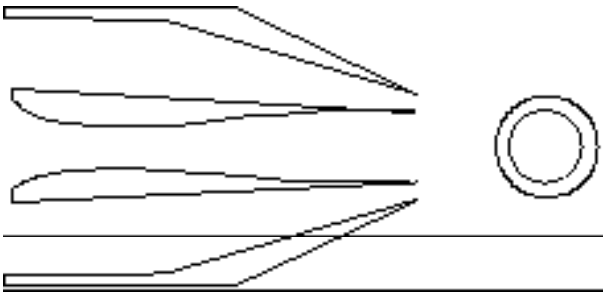

Fig. 1. Schematic of coaxial nozzle arrangement.

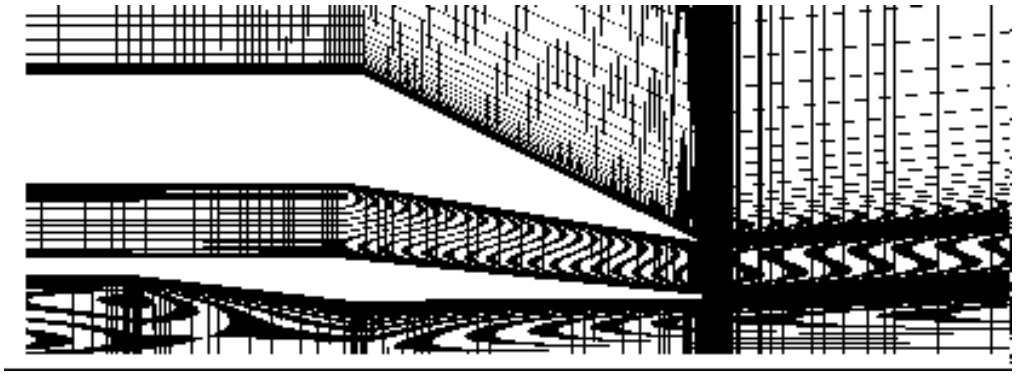

Fig. 2. Computational grid near nozzle exit for the C20 coaxial configuration.

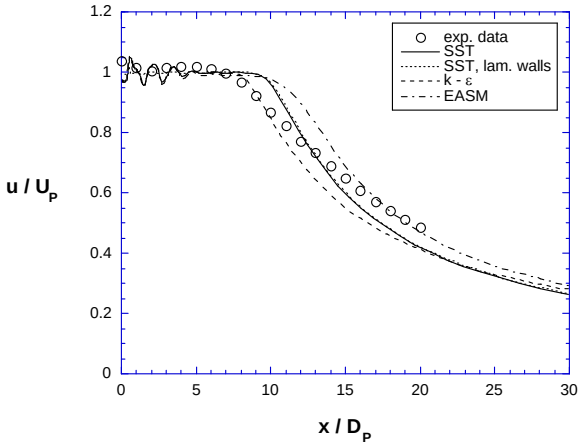

(a) centerline velocities

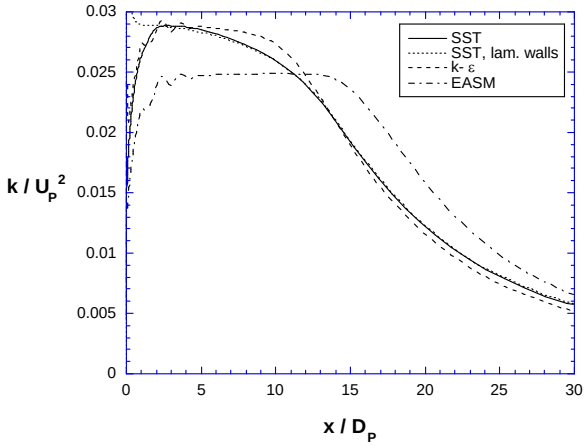

(b) maximum turbulent kinetic energy

Fig. 3. Turbulence model comparisons for single nozzle configuration.

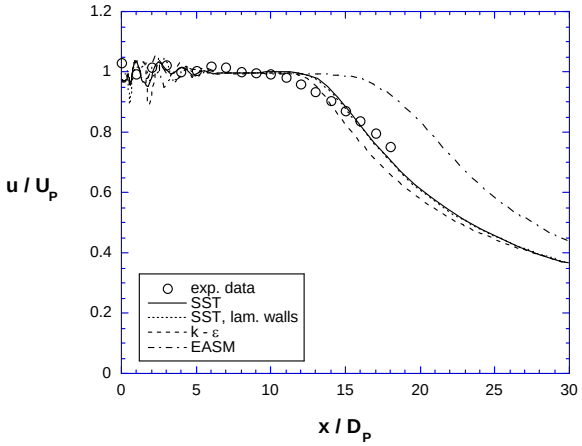

(a) centerline velocities

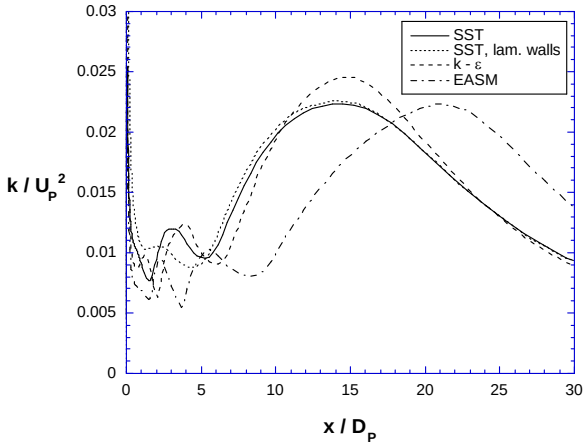

(b) maximum turbulent kinetic energy

Fig. 4. Turbulence model comparisons for C20M60 coaxial nozzle configuration.

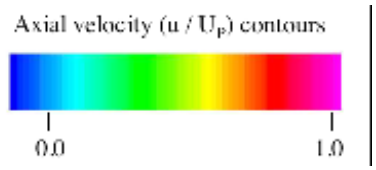

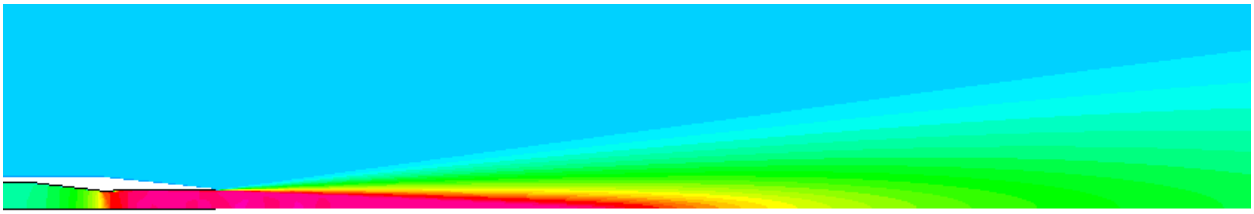

(a) Single jet

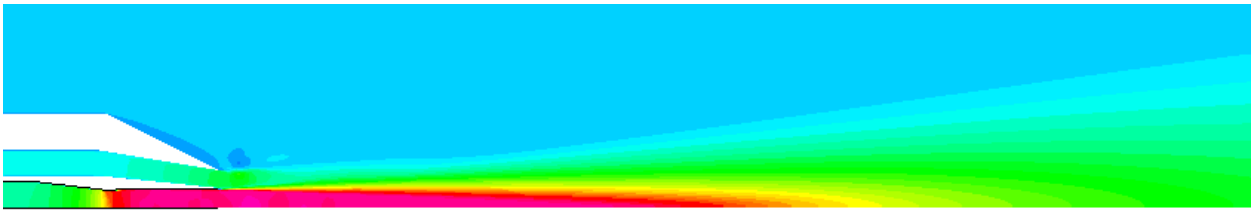

(b) C20M37

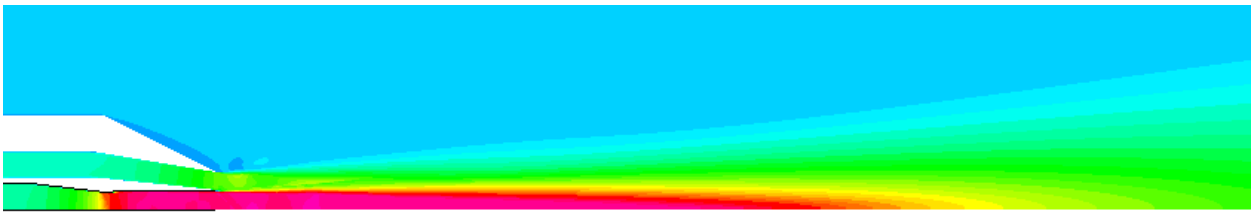

(c) C20M60

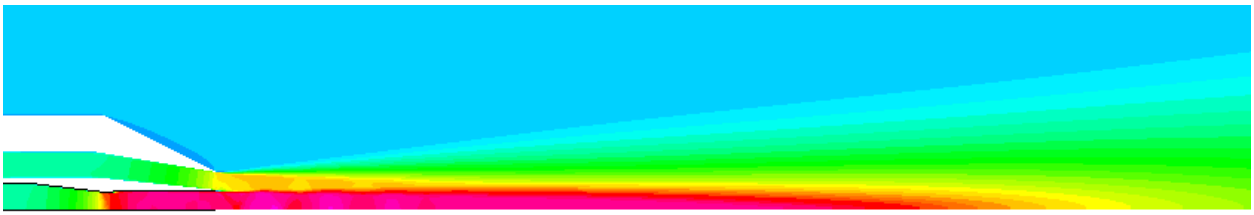

(d) C20M90

Fig. 5. Axial velocity contours for single and C20 coaxial nozzles.

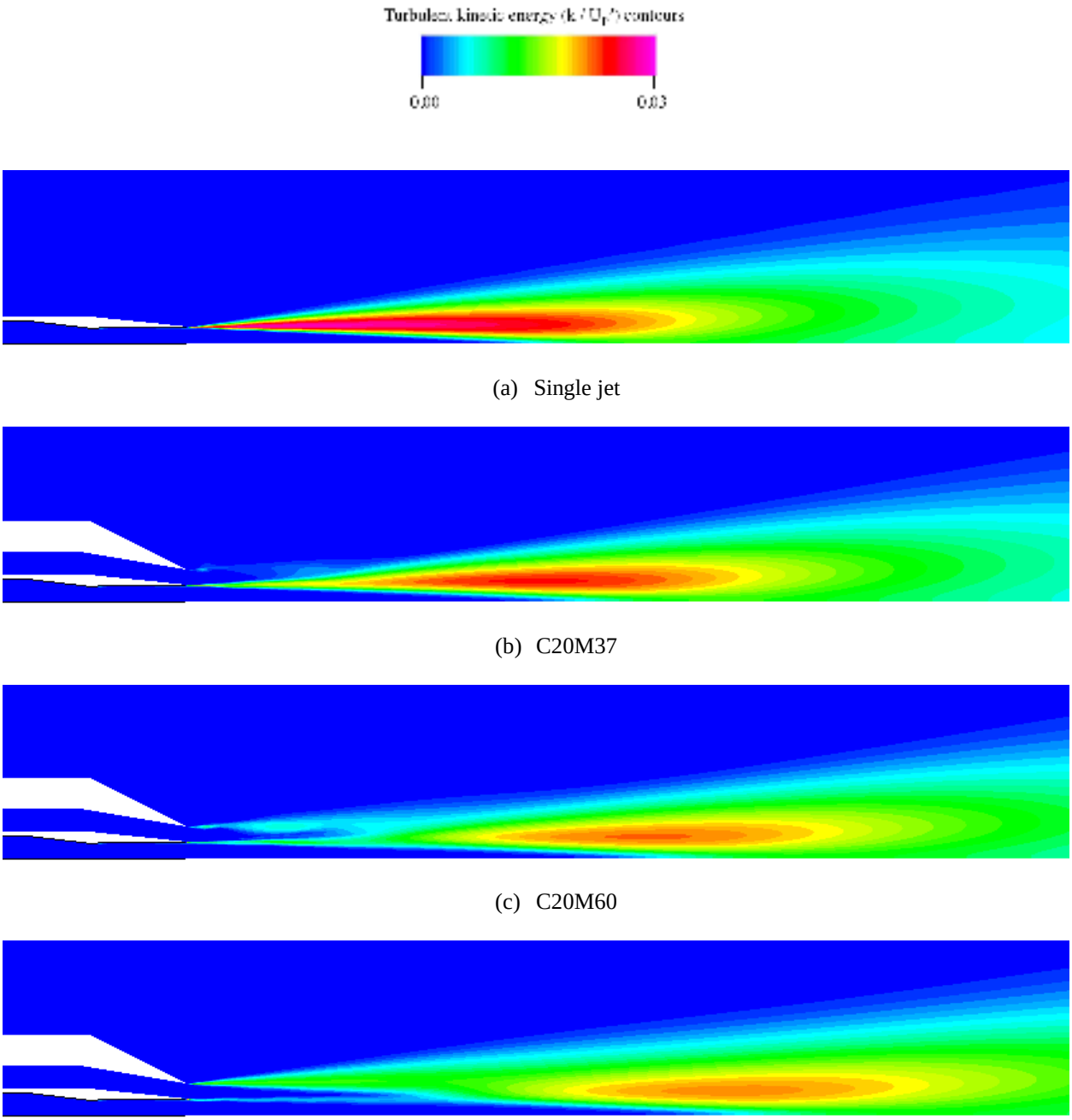

(a) Single jet

(b) C20M37

(c) C20M60

(d) C20M90

Fig. 6. Turbulent kinetic energy contours for single and C20 coaxial nozzles.

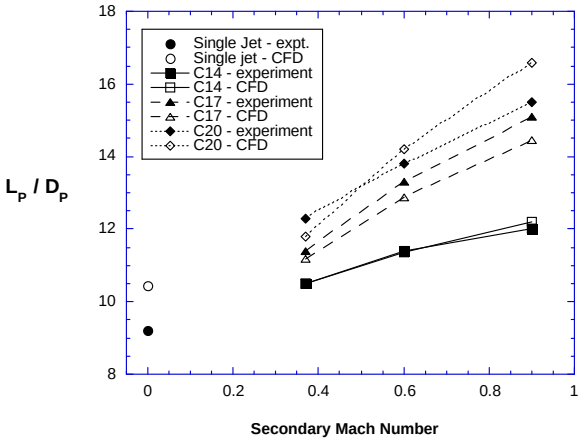

Fig. 7. Potential core lengths.

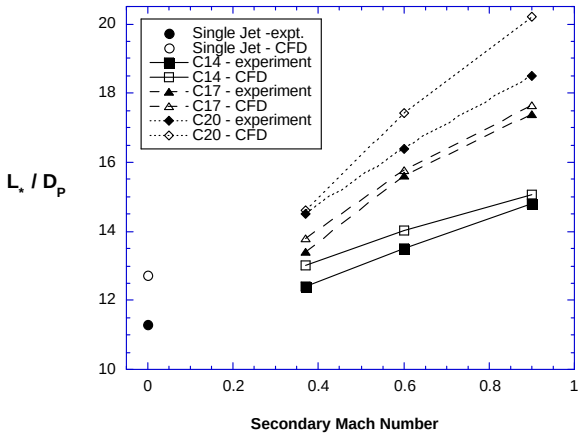

Fig. 8. Sonic lengths along centerline.

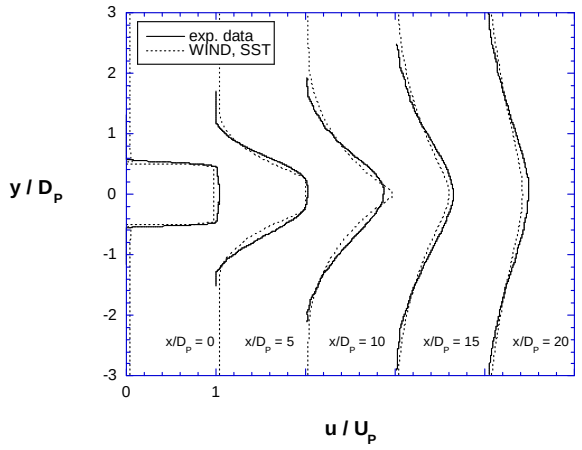

Fig. 9. Velocity profiles for single jet.

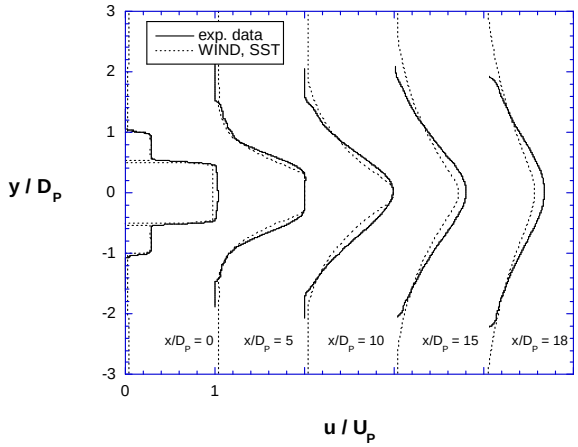

(a) Mach 0.37 secondary flow

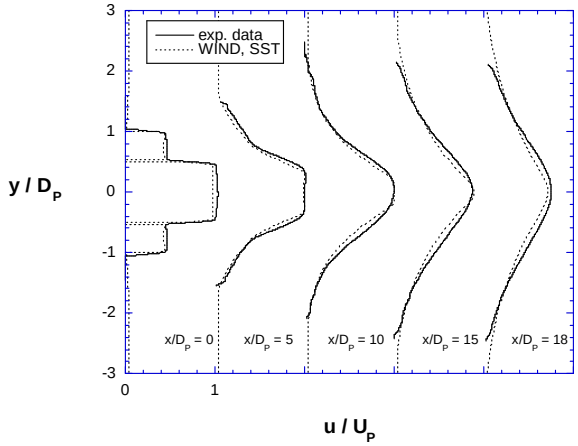

(b) Mach 0.60 secondary flow

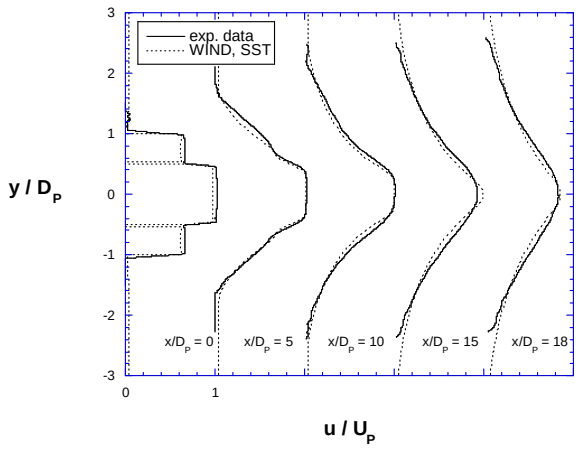

(c) Mach 0.90 secondary flow

Fig. 10. Velocity profiles for C20 coaxial jets.

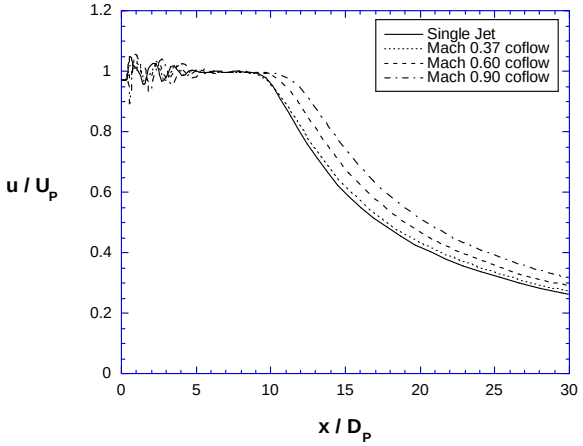

(a) C14 Coaxial nozzles

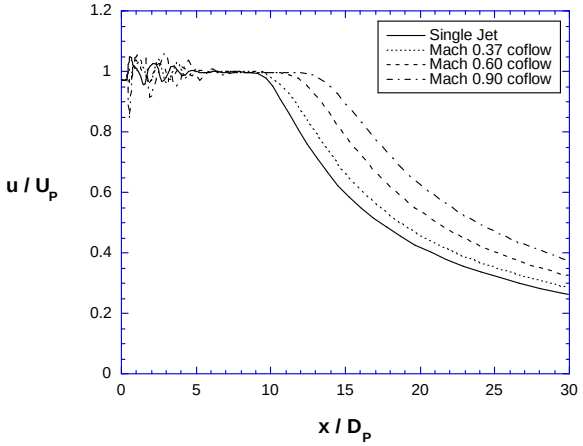

(b) C17 Coaxial nozzles

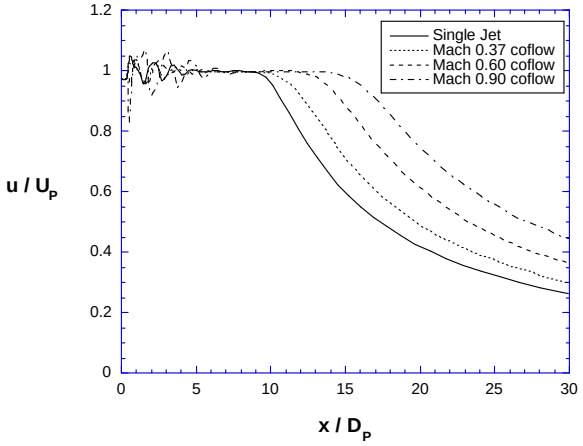

(c) C20 coaxial nozzles

Fig. 11. Centerline velocity variations for coaxial nozzles.

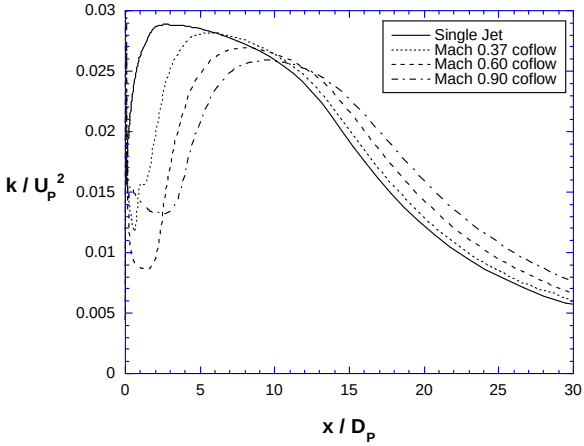

(a) C14 Coaxial nozzles

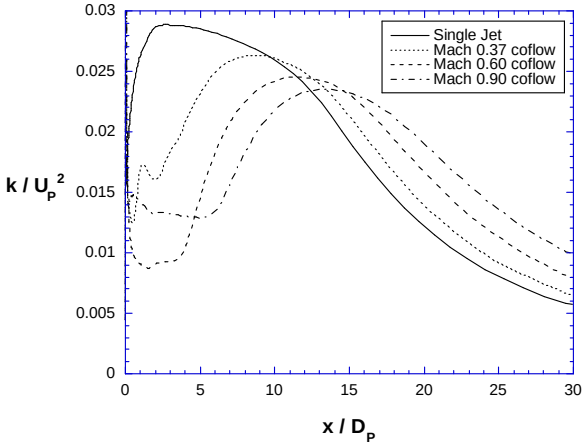

(b) C17 Coaxial nozzles

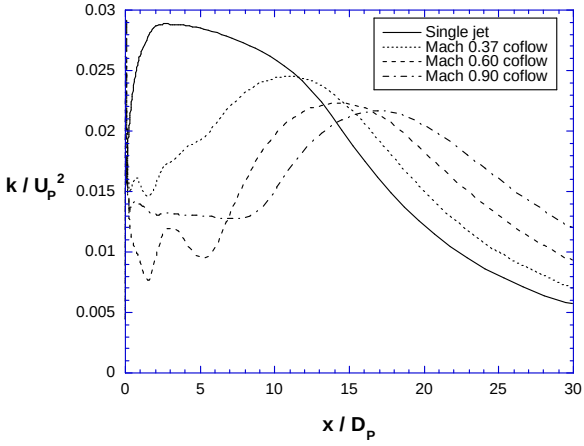

(c) C20 coaxial nozzles

Fig. 12. Maximum turbulent kinetic energy variations for coaxial nozzles.